Boundary integral methods applied to the analysis of diffractive optical elements

Dennis W. Prather

U.S. Army Research Laboratory, AMSRL-SE-EO, 2800 Powder Mill Road, Adelphi, Maryland 20783

Mark S. Mirotznik

The Catholic University of America, Department of Electrical Engineering, Washington, D.C. 20064

Joseph N. Mait

U.S. Army Research Laboratory, AMSRL-SE-EO, 2800 Powder Mill Road, Adelphi, Maryland 20783

Received March 8, 1996; revised manuscript received July 26, 1996; accepted August 9, 1996

We apply boundary integrals to the analysis of diffraction from both conductive and dielectric diffractive optical elements. Boundary integral analysis uses the integral form of the wave equation to describe the induced surface distributions over the boundary of a diffractive element. The surface distributions are used to determine the diffracted fields anywhere in space. In contrast to other vector analysis techniques, boundary integral methods are not restricted to the analysis of infinitely periodic structures but extend to finite aperiodic structures as well. We apply the boundary element method to solve the boundary integral equations and validate its implementation by comparing with analytical solutions our results for the diffractive analysis of a circular conducting cylinder and a dielectric cylinder. We also present the diffractive analysis of a conducting plate, a conducting linear grating, an eight-level off-axis conducting lens, an eight-level on-axis dielectric lens, and a binary dielectric lens that has subwavelength features. © 1997 Optical Society of America. [S0740-3232(97)01701-8]

1. INTRODUCTION

During the last three decades progress in the modeling and the design of diffractive optical elements (DOE's) has occurred primarily within the scalar domain.[1–6] This is due in part to the fact that scalar-based diffraction models can be applied to general structures, such as finite aperiodic and infinitely periodic DOE's, with relative ease. Although progress has been made in the vector analysis of DOE's,[7–14] it has been primarily limited to infinitely periodic structures. Thus, up till now, most references to the rigorous analysis of DOE's have implicitly assumed infinitely periodic elements, i.e., gratings, for which the eigenfunctions are known and are used in an eigenfunction expansion of the diffracted fields. However, for finite aperiodic elements, such as lenses and any physically realizable element, the eigenfunctions are not known, which precludes the application of eigenfunction expansion methods to such structures. To overcome this limitation, we consider the vector-based analysis of finite aperiodic DOE's by using a boundary integral method (BIM).

To the best of our knowledge, our work in this area represents the first application of BIMs to the vector-based diffraction analysis of finite aperiodic DOE's. In our previous work we presented the analysis of conducting DOE's[15]; our treatment here is more general and encompasses both perfectly conducting and homogeneous dielectric DOE's. For inhomogeneous DOE's volume integral methods[16,17] are better suited; for the structures addressed in this paper, however, BIM's require less computational effort and are consequently the preferred integral approach.

Boundary integral equations represent the integral form of the wave equation in terms of the induced surface distributions on the boundary of the DOE and can be applied to both finite aperiodic and infinitely periodic DOE's.[18–22] Once determined, the surface distributions can be used to calculate the diffracted field values anywhere in space. However, for all but a few structures, the boundary integral equations must be solved numerically.[23] We solve them by using the boundary element method (BEM).[24,25]

Alternative methods for the analysis of aperiodic DOE's have appeared in the literature and include the finite-difference (FD) method,[26] the finite-element method (FEM),[27] and the hybrid finite-element–boundary-element (FE-BE) method.[28] In the FD and FE methods a solution to the wave equation is determined within a finite-sized solution space. When these methods are applied to diffraction analysis, absorbing boundary conditions (ABC's) are necessary to make the solution space appear infinite. This minimizes the effect of nonphysical backreflections that result from the truncation of the solution space. Although for certain well-defined problems ABC's perform well, in general they can lead to unpredictable errors in the determination of the observed fields.[28–30] One can minimize this effect by extending the range of the solution space; however, this increases the computational effort and memory requirements needed in the analysis.[28]

0740-3232/97/010034-10$10.00

An advantage of BIM's over the FD and FE methods is that the radiation condition is satisfied implicitly within their formulation. Therefore BIM's do not require ABC's and thus are not subject to errors caused by nonphysical backreflections. However, boundary integral equations do require the construction of a suitable integral equation. Consequently, an exact Green's function must first be derived, which can be realized for homogeneous or discretely inhomogeneous media.

We are interested ultimately in the integration of DOE's with active components, e.g., microlasers, detectors, and modulators, for applications in optical interconnects and smart pixels. Depending upon the physical extent and profile of the diffractive structure, the solution of the boundary integral equations using the BEM can require extensive computational effort and significant memory requirements. The structures presented in this work, which range in width from approximately 5.0 to 42.0 wavelengths, were analyzed with a DEC station 5000 with 64 Mbytes of random access memory and 128 Mbytes of virtual memory.

We begin with an overview of the fundamental equations for BIM's in Section 2. Section 3 presents the application of BIM's to the analysis of conductive and dielectric DOE's that are finite and aperiodic. A summary and conclusions are presented in Section 4.

2. OVERVIEW OF BOUNDARY INTEGRAL METHODS

Although numerical solutions of the boundary integral equations are well known and have been applied extensively within the microwave community,[16,31] their application to the analysis of DOE's has been limited.[15] In this section we present the fundamental equations necessary for the application of BIM's to both conductive and dielectric DOE's. Although this material is covered in the references cited, we present it in more detail in Appendix A as an introduction for the DOE community.

Boundary integral equations relate the interaction between an incident field and a DOE by the use of distributions induced on the surface of the DOE by the incident field. For a conductor the surface distribution is a current, and for a dielectric it is a polarization field. Reradiation from the surface distribution, in turn, generates a diffracted field. Thus the objective in applying a BIM to the analysis of DOE's is to determine numerically the surface distributions given the incident field and the DOE.

In this presentation we assume that the incident field is a TE-polarized wave, in which case one need only consider the transverse component of the electric field; however, the method is completely general and can accommodate an arbitrary incident field. As shown in Fig. 1, the solution space is divided into two homogeneous regions: region I, which contains the DOE, and region O, which is free space. The boundary integral equations that describe the coupling between the scattered fields on the surface of the DOE and those in free space are[24,25]

$$0 = \mathbf{E}^{\mathrm{sc}}(\mathbf{r}_s)\left(1 - \frac{\theta}{2\pi}\right) + \fint_C \left[\mathbf{E}^{\mathrm{sc}}(\mathbf{r}')\frac{\partial G_I(\mathbf{r}_s, \mathbf{r}')}{\partial \hat{n}} - G_I(\mathbf{r}_s, \mathbf{r}')\frac{\partial \mathbf{E}^{\mathrm{sc}}(\mathbf{r}')}{\partial \hat{n}}\right] dl' + \mathbf{E}^{\mathrm{inc}}(\mathbf{r}_s)\left(1 - \frac{\theta}{2\pi}\right) + \fint_C \left[\mathbf{E}^{\mathrm{inc}}(\mathbf{r}')\frac{\partial G_I(\mathbf{r}_s, \mathbf{r}')}{\partial \hat{n}} - G_I(\mathbf{r}_s, \mathbf{r}')\frac{\partial \mathbf{E}^{\mathrm{inc}}(\mathbf{r}')}{\partial \hat{n}}\right] dl', \tag{1a}$$

$$0 = \mathbf{E}^{\mathrm{sc}}(\mathbf{r}_s)\left(\frac{\theta}{2\pi}\right) + \fint_C \left[G_O(\mathbf{r}_s, \mathbf{r}')\frac{\partial \mathbf{E}^{\mathrm{sc}}(\mathbf{r}')}{\partial \hat{n}} - \mathbf{E}^{\mathrm{sc}}(\mathbf{r}')\frac{\partial G_O(\mathbf{r}_s, \mathbf{r}')}{\partial \hat{n}}\right] dl', \tag{1b}$$

where $\fint$ is Cauchy's principal value of integration, $\mathbf{E}^{\mathrm{inc}}(\mathbf{r})$ and $\mathbf{E}^{\mathrm{sc}}(\mathbf{r})$ are the incident and scattered fields, respectively, $\mathbf{r}_s$ is a point on the DOE surface C, and $G_O(\mathbf{r}_s, \mathbf{r}')$ and $G_I(\mathbf{r}_s, \mathbf{r}')$ are the Green's functions for the regions O and I (see Fig. 1). The outward normal is $\hat{n}$, and θ is the angle exterior to region I subtended by the boundary in region O at the point $\mathbf{r}_s = \mathbf{r}'$, which is a point in the contour integral at which a singularity occurs. The total field $\mathbf{E}^{\mathrm{tot}}(\mathbf{r})$ is the sum of $\mathbf{E}^{\mathrm{inc}}(\mathbf{r})$ and $\mathbf{E}^{\mathrm{sc}}(\mathbf{r})$.

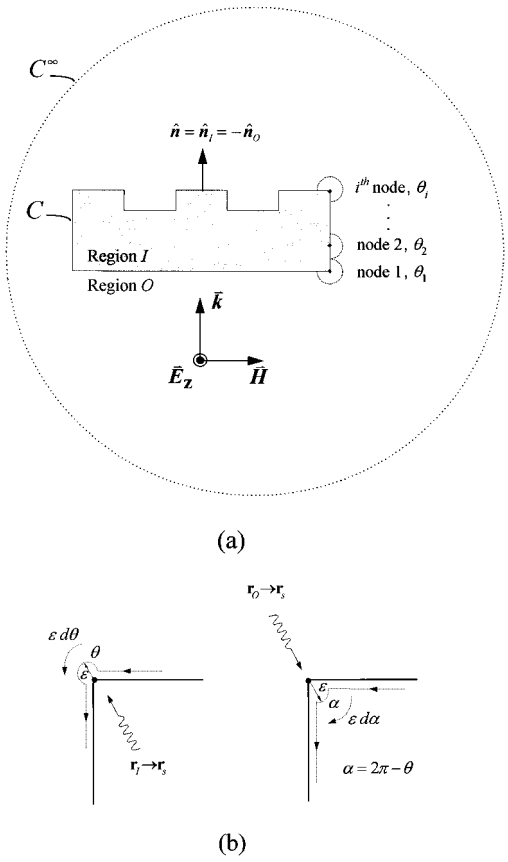

Fig. 1. Geometry used for boundary integral equations: (a) diffracting structure, (b) interior and exterior limiting contours.

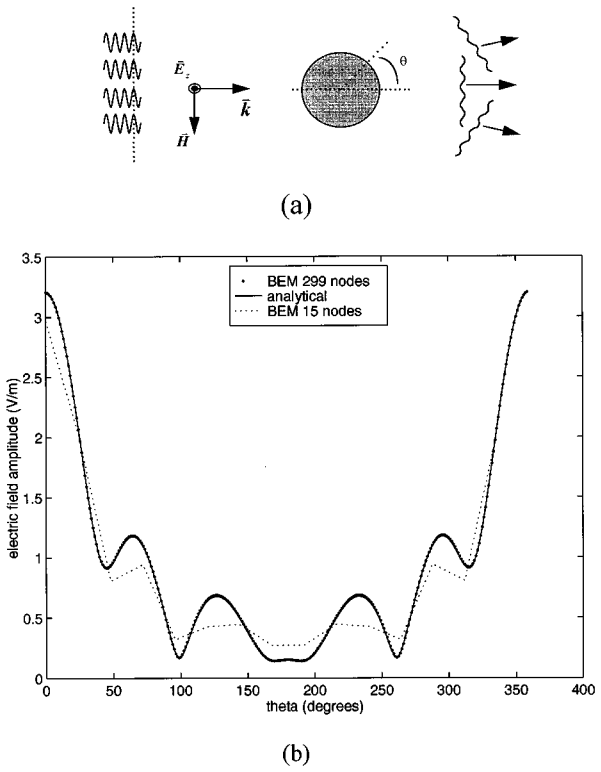

Fig. 2. Validation of BEM solution to boundary integral equations: (a) geometry of dielectric circular cylinder, (b) comparison of results generated by the BEM with analytical solution.

In the application of BIM's to perfect conductors Eqs. (1) reduce to a single integral equation in the exterior region:

$$\mathbf{E}^{\mathrm{sc}}(\mathbf{r}_s) = -\int_C \mathbf{Q}^{\mathrm{sc}}(\mathbf{r}')G_O(\mathbf{r}_s, \mathbf{r}')\mathrm{d}l'. \tag{2}$$

Equation (2) can be cast into the more familiar electric-field integral equation for perfect conductors:

$$\mathbf{E}^{\mathrm{inc}}(x_s, y_s) = \frac{\omega\mu}{4}\int_C \mathbf{J}(\mathbf{r}')G_O(\mathbf{r}_s, \mathbf{r}')\mathrm{d}l'. \tag{3}$$

To derive Eqs. (2) and (3), we have used the relationships $\mathbf{E}^{\mathrm{inc}}(\mathbf{r}_s) = -\mathbf{E}^{\mathrm{sc}}(\mathbf{r}_s)$ and $\mathbf{J}(\mathbf{r}') = (1/j\omega\mu)[\partial\mathbf{E}^{\mathrm{inc}}(\mathbf{r}')/\partial\hat{n}]$. The function $\mathbf{J}(\mathbf{r}')$ denotes the surface current density.

For all but a few structures the boundary integral equations (1) and (3) must be solved numerically.[23] We solve them by using the BEM.[24,25] An alternative technique for solving BIM's is the method of moments (MOM),[16,31] which has been applied extensively to the analysis of scattering and radiation problems in the microwave regime. However, unlike the MOM, the BEM expands the surface distributions by using *interpolation basis functions*,[24,25] whereas the MOM uses *scaled basis functions*.[16,31] In Section 3 we apply the BEM to solve numerically the boundary integral equations for the diffraction analysis of finite aperiodic DOE's. Derivation of the BEM is presented in Appendix B, again as an introduction for the DOE community.

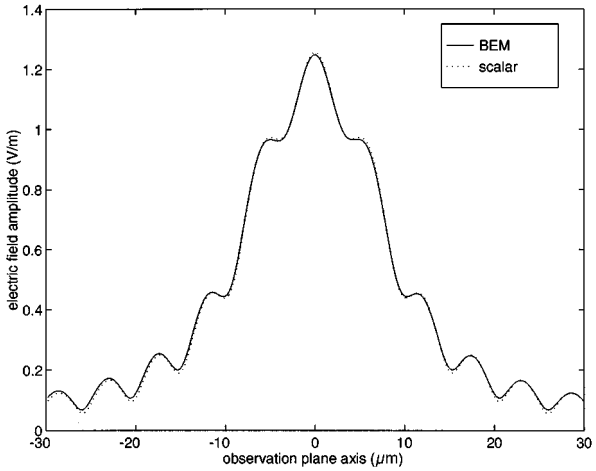

Fig. 3. Comparison of diffracted field determined by the BEM at 100λ from a perfectly conducting plate with that determined by scalar diffraction theory.

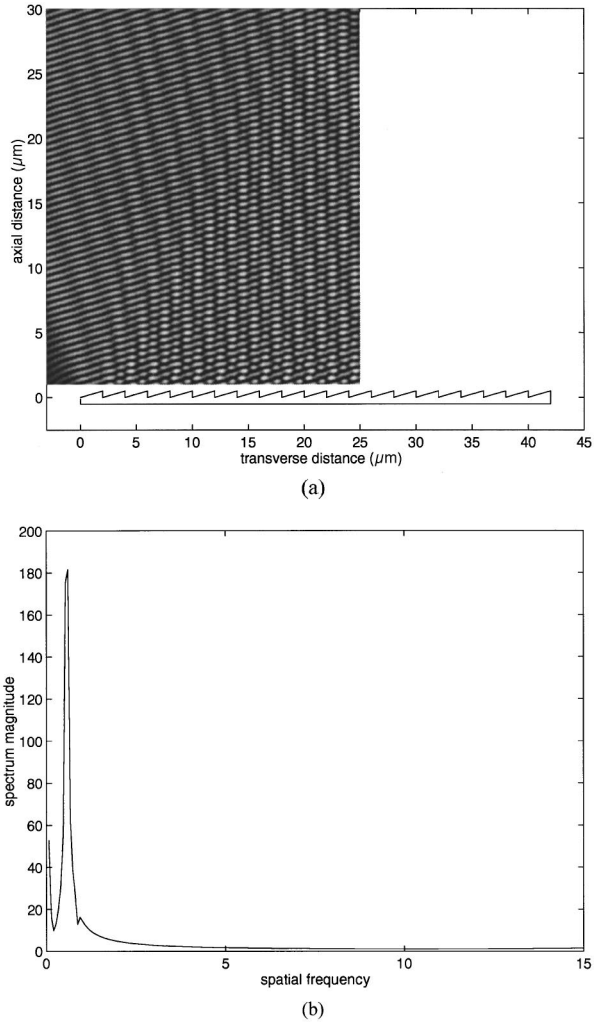

Fig. 4. Diffraction from a perfectly conducting grating: (a) regional plot of blazed grating and magnitude of electric field, (b) FFT of electric-field magnitude at a single plane in the far field.

3. NUMERICAL SIMULATIONS

In this section we present numerical simulations of finite periodic and aperiodic structures. The diffraction analysis of such structures is not possible with conventional vector-based diffraction models, i.e., rigorous coupled-wave[32] and coupled-mode[33–35] theories. In our simulations we assume a collimated uniform incident wave with TE polarization (the electric field perpendicular to the plane of incidence).

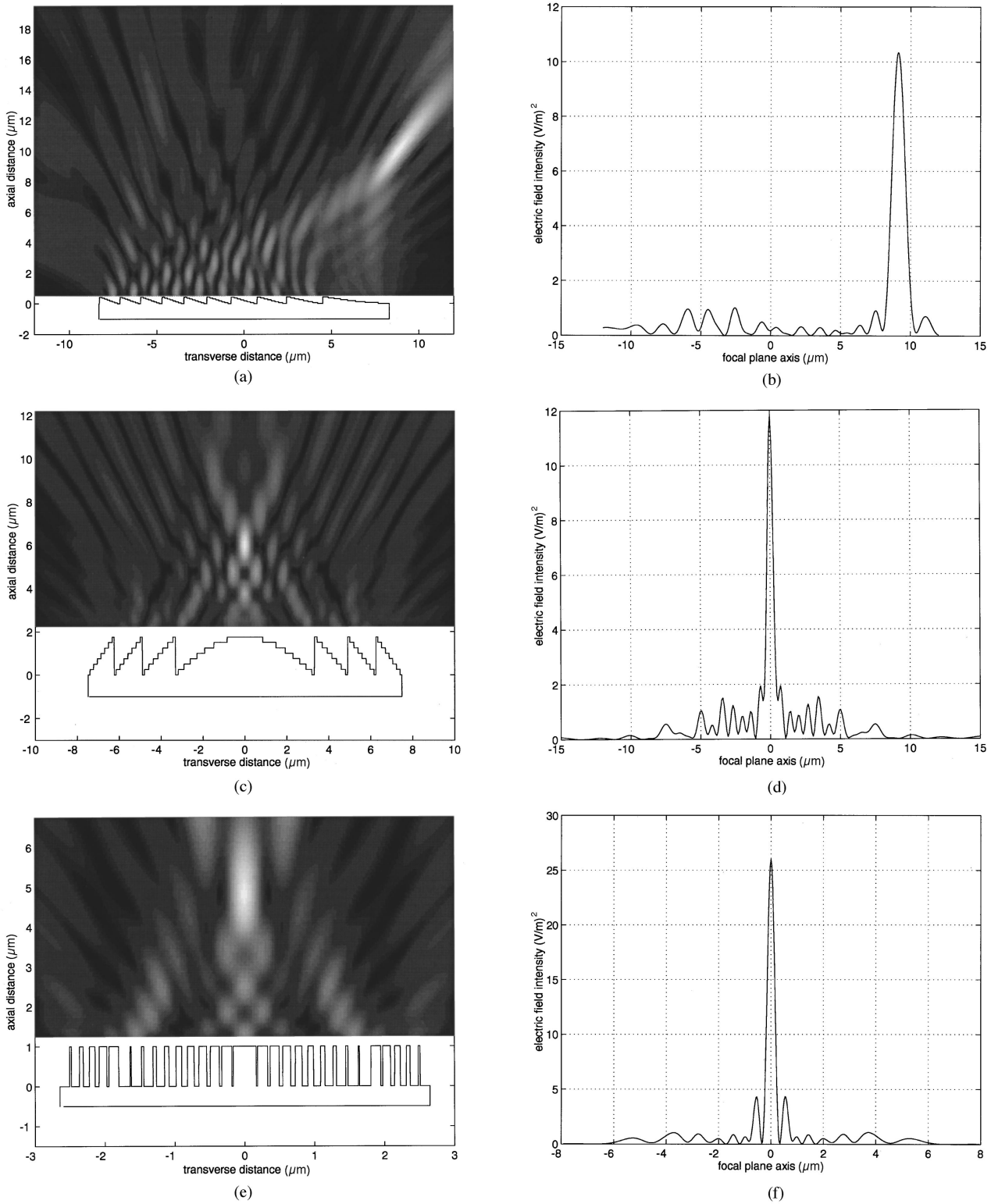

Fig. 5. Diffraction from diffractive lenses determined by the BEM. For a perfectly conducting off-axis lens (a) is a regional plot of electric-field magnitude, and (b) is a line scan of electric-field intensity in its focal plane. Plots (c) and (d) are the same as (a) and (b) but are for an on-axis dielectric lens. Plots (e) and (f) are the same as (a) and (b) but are for an on-axis dielectric lens that has subwavelength features.

Table 1. Design and Modeling Parameters for Conducting and Dielectric Diffractive Lenses

Lens	λ (μm)	Diameter (μm)	Focus (μm)	*f*/#	Levels	Nodes	Sampling Length
Off-axis conducting	1.0	16.60	10.0	0.600	8	662	λ/15.27
On-axis dielectric	1.0	14.96	5.0	0.334	8	865	λ/15.43
Subwavelength	0.5	5.29	3.0	0.567	2	1249	λ/17.97

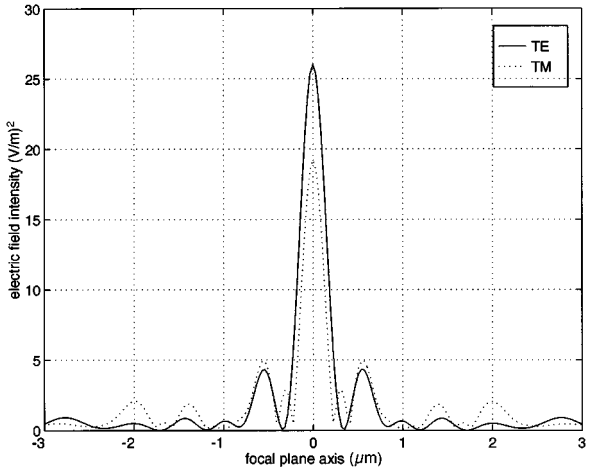

Fig. 6. Comparison of electric field magnitude in the focal plane of a subwavelength lens for TE and TM polarization.

Before applying our implementation to general diffractive structures, we first validated our models by comparing our analysis results with the analytical solution obtained for conducting and dielectric circular cylinders.[36] In addition, we compared our results for the far-field diffraction from a conducting plate with the solution predicted by scalar theory.

Figure 2(a) illustrates diffraction from a dielectric cylinder with an incident wavelength $\lambda = 1.0\ \mu$m. The cylinder, infinitely long with a radius 0.5 μm and a relative dielectric constant $\epsilon_r = 2.25$, was analyzed for both 299 nodes and 15 nodes, which correspond to sampling lengths of λ/47 and λ/2.4, respectively. Figure 2(b) is a comparison between the electric-field magnitude generated by the BEM and the analytically determined magnitude. For λ/47 sampling the root-mean-square (RMS) error is 0.057%, and for λ/2.4 sampling it is 18.88%. In general, we have determined that, for a RMS error of less than 5.0%, a minimum sampling length of λ/10 should be used. Similar results were obtained for the conducting cylinder.

We validated our conductor implementation of the BEM by using a 20.0 μm × 1.0 μm perfectly conducting plate. In the far field of this structure scalar theory is valid. Thus, in the limit, BEM results should agree with scalar theory. The boundary of the plate had 998 nodes, which corresponds to a sampling length of λ/23.7. Figure 3 is a comparison between the electric-field amplitude calculated at a distance of 100λ beyond the plate by the BEM and that predicted by scalar theory.[1] The RMS error is 1.16%.

Given the agreement between our implementation of the BEM and both analytical solutions and scalar-based models, we feel confident that it is a valid vector diffraction model that can be used to provide an accurate analysis of general diffractive structures. The DOE's that we consider include a conductive linear blazed grating, an eight-level off-axis conductive lens, an eight-level on-axis dielectric lens, and a dielectric lens that has subwavelength features. To design the subwavelength diffractive lens, we first approximated a continuous phase lens that had superwavelength features by a linear phase lens. We then replaced the linear phase segments by binary-phase subwavelength structures whose effective phase is approximately linear.[7]

The conductive finite periodic linear blazed grating is shown in Fig. 4(a). In this figure, as well as Figs. 5(a), 5(c), and 5(e), the bright regions correspond to high field values, and the dark regions correspond to low values. We designed the grating for 100% diffraction efficiency into the first order by using scalar theory. The number of boundary nodes on the grating boundary is 989, which corresponds to a sampling length of λ/10.2. Figure 4(b) is the fast Fourier transform (FFT) of a line scan taken in the far field of the grating. The FFT indicates a single spatial frequency, consistent with our design.

The results of our application of the BEM to different lens structures are presented in Fig. 5. The parameters used in the analysis are summarized in Table 1. The conducting lens has a maximum etch depth of $7\lambda/16 = 0.437\ \mu$m, and the dielectric lens has a maximum etch depth of $7\lambda/8(n-1) = 1.75\ \mu$m, where $n = \sqrt{\epsilon_r} = \sqrt{2.25}$. Figures 5(a), 5(c), and 5(e) are regional plots of the off-axis conducting, on-axis dielectric, and subwavelength lenses, respectively. Figures 5(b), 5(d), and 5(e) show line scans through the focal planes of the respective lenses. Our results reflect the focal shift for lenses that have low Fresnel numbers; thus the maximum intensity actually occurred at a plane closer to the lens than the focal plane.[37] Figure 6 is a line scan through the focal plane of the subwavelength lens for both TE and TM polarization and illustrates the polarization dependence of the subwavelength structure's form birefringence.

4. CONCLUSION

We have demonstrated and applied a general BIM to model the vector diffraction from finite aperiodic DOE's. The diffraction analysis of the structures presented in this paper is not possible with conventional vector-based diffraction models, i.e., rigorous coupled-wave and coupled-mode theories. BIM's can also be applied to infinitely periodic DOE's and can therefore be applied to

more general structures than can conventional methods. In addition, boundary integrals implicitly satisfy the radiation conditions and therefore do not require ABC's as in the FD and FE methods.

We solved the BIM's by using the BEM, validated their implementation by comparing our analysis with analytical solutions, and applied them to the analysis of a conductive linear grating, eight-level off-axis conductive and on-axis dielectric lenses, and a subwavelength lens. However, the ultimate objective of our work is the synthesis, or the design, of diffractive elements using vector-based diffraction models. To this end, we are currently exploring BIM's and other techniques.

APPENDIX A

In this appendix we present as a review the formulation of the boundary integral equations and their solution using the BEM. The equations are cast into matrix form for ease of computer implementation.

We consider the boundary integral equations for a two-dimensional diffractive structure that is uniform in the z direction. The analysis presented below assumes an incident field that has TE polarization, in which case one need only consider the z component of the electric field. However, this technique can be applied to TM polarization as well. Also, this analysis can include imperfect conductors, in which case the permittivity of the interior region ϵ_I is complex, $\epsilon_I = \epsilon_r\epsilon_O + j\sigma/\omega$, where σ denotes electrical conductivity.

We formulate the boundary integral equations by separating the solution space into discretely homogeneous regions. For a phase-only DOE located in free space there are two regions: region I, which contains the DOE, and region O, which is free space, as shown in Fig. 1(a) in the main body of the paper. Within each region the two-dimensional time-harmonic wave equation is applied. In the interior region the homogeneous wave equation applies; however, in the exterior region (where the incident wave is assumed to originate), an inhomogeneous wave equation must be solved:

$$\begin{aligned} 0 &= \nabla^2\mathbf{E}^{\text{tot}}(\mathbf{r}) + \beta_I{}^2\mathbf{E}^{\text{tot}}(\mathbf{r}) \qquad \text{for} \quad \mathbf{r} \in I, \\ -f(\mathbf{r}) &= \nabla^2\mathbf{E}^{\text{tot}}(\mathbf{r}) + \beta_O{}^2\mathbf{E}^{\text{tot}}(\mathbf{r}) \qquad \text{for} \quad \mathbf{r} \in O, \end{aligned} \tag{A1}$$

where $\beta_I = 2\pi\sqrt{\epsilon_r}/\lambda$, $\beta_O = 2\pi/\lambda$, and $f(\mathbf{r})$ represents the source term. Equations (A1) are cast in the form of boundary integral equations by the application of Green's second identity[21,31]:

$$\begin{aligned} \mathbf{E}^{\text{tot}}(\mathbf{r}) = \int_C \Bigg[& G_I(\mathbf{r}, \mathbf{r}')\frac{\partial\mathbf{E}^{\text{tot}}(\mathbf{r}')}{\partial\hat{n}} \\ & - \mathbf{E}^{\text{tot}}(\mathbf{r}')\frac{\partial G_I(\mathbf{r}, \mathbf{r}')}{\partial\hat{n}}\Bigg] dl', \qquad \mathbf{r} \in I, \end{aligned}$$

$$\begin{aligned} \mathbf{E}^{\text{tot}}(\mathbf{r}) = \mathbf{E}^{\text{inc}}(\mathbf{r}) + \left(\int_C + \int_{C^\infty} \right) & \\ \times \Bigg[& \mathbf{E}^{\text{tot}}(\mathbf{r}')\frac{\partial G_O(\mathbf{r}, \mathbf{r}')}{\partial\hat{n}} \\ & - G_O(\mathbf{r}, \mathbf{r}')\frac{\partial\mathbf{E}^{\text{tot}}(\mathbf{r}')}{\partial\hat{n}}\Bigg] dl', \qquad \mathbf{r} \in O, \end{aligned} \tag{A2}$$

where $\mathbf{E}^{\text{tot}}(\mathbf{r})$ and

$$\mathbf{E}^{\text{inc}}(\mathbf{r}) = \int_{C^\infty} f(\mathbf{r}')G_O(\mathbf{r}, \mathbf{r}')dl' \tag{A3}$$

are the total and incident electric-field vectors, respectively. The position vector $\mathbf{r}(x, y)$ is a vector from the origin to the observation point, and $\mathbf{r}'(x', y')$ is a vector from the origin to the source point. A minus sign is introduced because $\hat{n} = \hat{n}_I = -\hat{n}_O$. The contours C and C^∞ represent the contours of the DOE and a fictitious contour at infinity, respectively. The two-dimensional free-space Green's functions are

$$\begin{aligned} G_I(\mathbf{r}, \mathbf{r}') &= \frac{1}{4j}H_0^{(2)}(\beta_I|\mathbf{r} - \mathbf{r}'|) \\ &= \frac{1}{4j}H_0^{(2)}\left[\beta_I\sqrt{(x - x')^2 + (y - y')^2}\right], \\ G_O(\mathbf{r}, \mathbf{r}') &= \frac{1}{4j}H_0^{(2)}(\beta_O|\mathbf{r} - \mathbf{r}'|) \\ &= \frac{1}{4j}H_0^{(2)}\left[\beta_O\sqrt{(x - x')^2 + (y - y')^2}\right], \end{aligned} \tag{A4}$$

where $H_0{}^{(2)}(\beta|\mathbf{r} - \mathbf{r}'|)$ is the zero-order Hankel function of the second kind.

We solve Eqs. (A2) by confining the observation vector to the contour C of the DOE, i.e., $\mathbf{r} = \mathbf{r}_s$, and by expressing the total electric field in terms of the incident $[\mathbf{E}^{\text{inc}}(\mathbf{r})]$ and scattered $[\mathbf{E}^{\text{sc}}(\mathbf{r})]$ fields:

$$\mathbf{E}^{\text{tot}}(\mathbf{r}) = \mathbf{E}^{\text{inc}}(\mathbf{r}) + \mathbf{E}^{\text{sc}}(\mathbf{r}). \tag{A5}$$

By formulating the boundary integral equations in terms of the scattered fields, we can avoid numerical errors that result when the frequency of the illumination wavelength is a resonant frequency of the structure. Such errors are known to occur when the boundary integral equations are applied to closed boundaries.[38] If we substitute Eq. (A5) into Eqs. (A2) and incorporate the Sommerfeld radiation condition,

$$\int_{C^\infty}\left[G_O(\mathbf{r}, \mathbf{r}')\frac{\partial\mathbf{E}^{\text{sc}}(\mathbf{r}')}{\partial\hat{n}} - \mathbf{E}^{\text{sc}}(\mathbf{r}')\frac{\partial G_O(\mathbf{r}, \mathbf{r}')}{\partial\hat{n}}\right] dl' = 0, \qquad \mathbf{r} \in O, \tag{A6}$$

and the extinction theorem,

$$\int_C \left[G_O(\mathbf{r}, \mathbf{r}') \frac{\partial \mathbf{E}^{\text{inc}}(\mathbf{r}')}{\partial \hat{n}} - \mathbf{E}^{\text{inc}}(\mathbf{r}') \frac{\partial G_O(\mathbf{r}, \mathbf{r}')}{\partial \hat{n}} \right] dl' = 0, \quad \mathbf{r} \in O, \tag{A7}$$

we have

$$\begin{aligned} 0 = \mathbf{E}^{\text{sc}}(\mathbf{r}_s) + \int_C \Bigg[& \mathbf{E}^{\text{sc}}(\mathbf{r}') \frac{\partial G_I(\mathbf{r}_s, \mathbf{r}')}{\partial \hat{n}} \\ & - G_I(\mathbf{r}_s, \mathbf{r}') \frac{\partial \mathbf{E}^{\text{sc}}(\mathbf{r}')}{\partial \hat{n}} \Bigg] dl' + \mathbf{E}^{\text{inc}}(\mathbf{r}_s) \\ & + \int_C \left[\mathbf{E}^{\text{inc}}(\mathbf{r}') \frac{\partial G_I(\mathbf{r}_s, \mathbf{r}')}{\partial \hat{n}} - G_I(\mathbf{r}_s, \mathbf{r}') \frac{\partial \mathbf{E}^{\text{inc}}(\mathbf{r}')}{\partial \hat{n}} \right] dl', \end{aligned}$$

$$0 = \mathbf{E}^{\text{sc}}(\mathbf{r}_s) + \int_C \left[G_O(\mathbf{r}_s, \mathbf{r}') \frac{\partial \mathbf{E}^{\text{sc}}(\mathbf{r}')}{\partial \hat{n}} - \mathbf{E}^{\text{sc}}(\mathbf{r}') \frac{\partial G_O(\mathbf{r}_s, \mathbf{r}')}{\partial \hat{n}} \right] dl'. \tag{A8}$$

Care must be exercised when evaluating Eqs. (A8) because of singularities that exist when $\mathbf{r}_s = \mathbf{r}'$. We evaluate these singularities by integrating around the singularity in the limit as $\mathbf{r}'$ approaches $\mathbf{r}_s$ [see Fig. 1(b)]. For the outside region this results in

$$\begin{aligned} 0 = \mathbf{E}^{\text{sc}}(\mathbf{r}_s) - \fint_C & \left[\mathbf{E}^{\text{sc}}(\mathbf{r}') \frac{\partial G_O(\mathbf{r}_s, \mathbf{r}')}{\partial \hat{n}} - G_O(\mathbf{r}_s, \mathbf{r}') \frac{\partial \mathbf{E}^{\text{sc}}(\mathbf{r}')}{\partial \hat{n}} \right] dl' - \lim_{\varepsilon \to 0} \left\{ \int_{-\alpha/2}^{\alpha/2} \left[-\frac{\mathbf{E}^{\text{sc}}(\mathbf{r}')}{2\pi\varepsilon} \right. \right. \\ & \left. \left. + \frac{\ln(\beta_O \varepsilon)}{2\pi} \frac{\partial E^{\text{sc}}(\mathbf{r}')}{\partial \hat{n}} \right] \varepsilon \, d\theta \right\}, \end{aligned} \tag{A9}$$

where $\fint$ is Cauchy's principal value of integration and we have used the small-argument approximation for Hankel functions.[39] As shown in Fig. 1(b), $\mathbf{E}^{\text{sc}}(\mathbf{r}_s)$ and α are the scattered field and the exterior angle subtended by the boundary at the observation point $\mathbf{r}_s$ and

$$\varepsilon = \lim_{\mathbf{r}' \to \mathbf{r}_s} |\mathbf{r}_s - \mathbf{r}'|. \tag{A10}$$

The singularity for the interior region I is evaluated in a similar fashion. For the exterior integral equation the angle of integration α, as shown in Fig. 1(b), represents the complement to the angle used in the interior integral equation, θ; thus the relationship $\alpha = 2\pi - \theta$ must be used. The resulting boundary integral equations are

$$\begin{aligned} 0 = \mathbf{E}^{\text{sc}}(\mathbf{r}_s) & \left(1 - \frac{\theta}{2\pi} \right) + \fint_C \left[\mathbf{E}^{\text{sc}}(\mathbf{r}') \frac{\partial G_I(\mathbf{r}_s, \mathbf{r}')}{\partial \hat{n}} - G_I(\mathbf{r}_s, \mathbf{r}') \frac{\partial \mathbf{E}^{\text{sc}}(\mathbf{r}')}{\partial \hat{n}} \right] dl' + \mathbf{E}^{\text{inc}}(\mathbf{r}_s) \left(1 - \frac{\theta}{2\pi} \right) \\ & + \fint_C \left[\mathbf{E}^{\text{inc}}(\mathbf{r}') \frac{\partial G_I(\mathbf{r}_s, \mathbf{r}')}{\partial \hat{n}} - G_I(\mathbf{r}_s, \mathbf{r}') \frac{\partial \mathbf{E}^{\text{inc}}(\mathbf{r}')}{\partial \hat{n}} \right] dl', \end{aligned}$$

$$0 = \mathbf{E}^{\text{sc}}(\mathbf{r}_s) \left(\frac{\theta}{2\pi} \right) + \fint_C \left[G_O(\mathbf{r}_s, \mathbf{r}') \frac{\partial \mathbf{E}^{\text{sc}}(\mathbf{r}')}{\partial \hat{n}} - \mathbf{E}^{\text{sc}}(\mathbf{r}') \frac{\partial G_O(\mathbf{r}_s, \mathbf{r}')}{\partial \hat{n}} \right] dl'. \tag{A11}$$

Equations (A11) represent Eqs. (1a) and (1b) in Section 2. Once determined, the scattered electric field $\mathbf{E}^{\text{sc}}(\mathbf{r}')$ and its normal derivative $\partial \mathbf{E}^{\text{sc}}(\mathbf{r}')/\partial \hat{n}$ are used to calculate the scattered fields anywhere in space by

$$\mathbf{E}^{\text{sc}}(\mathbf{r}) = \int_C \left[\mathbf{E}^{\text{sc}}(\mathbf{r}') \frac{\partial G_O(\mathbf{r}, \mathbf{r}')}{\partial \hat{n}} - G_O(\mathbf{r}, \mathbf{r}') \frac{\partial \mathbf{E}^{\text{sc}}(\mathbf{r}')}{\partial \hat{n}} \right] dl', \tag{A12}$$

where $\mathbf{r} \in O$.

In Appendix B we present the solution of Eqs. (A11) using the BEM.

APPENDIX B

The BEM presented here is completely general and allows for the analysis of finite and aperiodic structures. The application of the BEM to dielectric and conducting DOE's is treated separately in the following subsections.

A. Boundary Electric Method for Dielectric Diffractive Optical Elements

In the application of the BEM to dielectrics we solve the coupled integral equations in Eqs. (A11) by expanding the unknown surface distributions, the scattered electric field, $\mathbf{E}^{\text{sc}}(\mathbf{r}')$, and its normal derivative, $\partial \mathbf{E}^{\text{sc}}(\mathbf{r}')/\partial \hat{n}$, in terms of interpolation functions:

$$\begin{aligned} \mathbf{E}^{\text{sc}}[\mathbf{r}'(\xi)] &= \sum_{n=1}^{N} \hat{E}_n^{\text{sc}}(\xi) = \sum_{n=1}^{N} E_n^{\text{sc}} \phi_1(\xi) + E_{n+1}^{\text{sc}} \phi_2(\xi), \\ \frac{\partial \mathbf{E}^{\text{sc}}[\mathbf{r}'(\xi)]}{\partial \hat{n}} &= \mathbf{Q}^{\text{sc}}[\mathbf{r}'(\xi)] = \sum_{n=1}^{N} \hat{Q}_n^{\text{sc}}(\xi) \\ &= \sum_{n=1}^{N} Q_n^{\text{sc}} \phi_1(\xi) + Q_{n+1}^{\text{sc}} \phi_2(\xi). \end{aligned} \tag{B1}$$

When $n = N$, node 1 is replaced with $n + 1$. The interpolation functions $\phi_1(\xi)$ and $\phi_2(\xi)$ are defined over a single elemental segment. In this analysis linear interpolation functions are used:

$$\phi_1(\xi) = (1 - \xi)/2, \qquad \phi_2(\xi) = (1 + \xi)/2, \tag{B2}$$

where $\xi = [-1, 1]$. However, higher-order interpolation functions can also be used.[25] In this notation the contour of the DOE is represented by a local coordinate transformation, $\mathbf{r}'(\xi) = \mathbf{r}'[\hat{x}_n(\xi), \hat{y}_n(\xi)]$, where

$$\hat{x}_n(\xi) = x_n\phi_1(\xi) + x_{n+1}\phi_2(\xi),$$

$$\hat{y}_n(\xi) = y_n\phi_1(\xi) + y_{n+1}\phi_2(\xi). \tag{B3}$$

The nodal values (x_n, y_n) and (x_{n+1}, y_{n+1}) represent the sample points on the boundary, and $\hat{x}_n(\xi)$ and $\hat{y}_n(\xi)$ are interpolated coordinate values between nodes. In this formulation the nodal values must be numbered in a sequential counterclockwise fashion.

Substitution of Eqs. (B1) into Eqs. (A11) yields a system of two equations in $2N$ unknowns. To generate $2N$ equations in $2N$ unknowns, we performed an inner product between both sides of Eqs. (A11) with a set of N weighting functions. In this analysis the weighting functions are Dirac-delta functions that sample the boundary of the DOE:

$$\omega_m = \delta[\mathbf{r}'(\xi) - \mathbf{r}'_m] = \begin{cases} 1, & \mathbf{r}'(\xi) = \mathbf{r}'_m \\ 0, & \text{elsewhere} \end{cases}, \tag{B4}$$

where $m = 1, 2, \ldots, N$ and $\mathbf{r}'_m$ is a set of N position vectors along the contour C of the DOE. This approach is referred to as point matching.

Substituting Eqs. (B1) and (B2) into Eqs. (A11) and performing an inner product between ω_m yields a set of linear algebraic equations:

$$\begin{bmatrix} ZI_{n,m} & -YI_{n,m} \\ ZO_{n,m} & YO_{n,m} \end{bmatrix} \begin{bmatrix} E_m^{\text{sc}} \\ Q_m^{\text{sc}} \end{bmatrix} = \begin{bmatrix} -ZI_{n,m} & YI_{n,m} \\ 0 & 0 \end{bmatrix} \begin{bmatrix} E_m^{\text{inc}} \\ Q_m^{\text{inc}} \end{bmatrix}, \tag{B5}$$

where

$$ZI_{n,m} = \left(1 - \frac{\theta_n}{2\pi}\right)\delta_{nm} + \int_{-1}^{1} \left\{ \frac{\Delta l_n}{2}\phi_1(\xi)\frac{\partial G_I[\mathbf{r}'(\hat{x}_n, \hat{y}_n), \mathbf{r}'_m]}{\partial \hat{n}} + \frac{\Delta l_{n-1}}{2}\phi_2(\xi)\frac{\partial G_I[\mathbf{r}'(\hat{x}_{n-1}, \hat{y}_{n-1}), \mathbf{r}'_m]}{\partial \hat{n}} \right\} \mathrm{d}\xi,$$

$$YI_{n,m} = \int_{-1}^{1} \left\{ \frac{\Delta l_n}{2}\phi_1(\xi)G_I[\mathbf{r}'(\hat{x}_n, \hat{y}_n), \mathbf{r}'_m] + \frac{\Delta l_{n-1}}{2}\phi_2(\xi)G_I[\mathbf{r}'(\hat{x}_{n-1}, \hat{y}_{n-1}), \mathbf{r}'_m] \right\} \mathrm{d}\xi,$$

$$ZO_{n,m} = \left(\frac{\theta_n}{2\pi}\right)\delta_{nm} - \int_{-1}^{1} \left\{ \frac{\Delta l_n}{2}\phi_1(\xi)\frac{\partial G_O[\mathbf{r}'(\hat{x}_n, \hat{y}_n), \mathbf{r}'_m]}{\partial \hat{n}} + \frac{\Delta l_{n-1}}{2}\phi_2(\xi)\frac{\partial G_O[\mathbf{r}'(\hat{x}_{n-1}, \hat{y}_{n-1}), \mathbf{r}'_m]}{\partial \hat{n}} \right\} \mathrm{d}\xi,$$

$$YO_{n,m} = \int_{-1}^{1} \left\{ \frac{\Delta l_n}{2}\phi_1(\xi)G_O[\mathbf{r}'(\hat{x}_n, \hat{y}_n), \mathbf{r}'_m] + \frac{\Delta l_{n-1}}{2}\phi_2(\xi)G_O[\mathbf{r}'(\hat{x}_{n-1}, \hat{y}_{n-1}), \mathbf{r}'_m] \right\} \mathrm{d}\xi. \tag{B6}$$

In addition, $\mathrm{d}\xi = 2\mathrm{d}l'/\Delta l_n$, $E_m^{\text{inc}} = E^{\text{inc}}(x_m, y_m)$, $Q_m^{\text{inc}} = \partial E_m^{\text{inc}}(\mathbf{r}')/\partial\hat{n}$, and Δl_n represents the length of the corresponding line segment for element n. The integral equations in Eqs. (B6) specify a unique relationship between the electric field and its normal derivative at each node on the boundary to each and every other node on the boundary; i.e., they impose the boundary-value problem.

Once the solution to Eq. (B5) is determined, one can use Eq. (A12) to calculate the scattered field values at any observation point. To produce the total diffracted field, the incident field is added to the scattered field in the observation plane. In our analysis the incident wave was propagated to the observation plane by Rayleigh–Sommerfeld diffraction.[1]

The above analysis was performed for TE polarization (electric field perpendicular to the plane of incidence). However, this technique is also valid for TM polarization, in which case Eqs. (A1) are formulated in terms of the magnetic-field (H_z) component. The TM analysis follows the above procedure, and the resulting system of equations is

$$\begin{bmatrix} ZI_{n,m} & -\epsilon_{r,1}YI_{n,m} \\ ZO_{n,m} & \epsilon_{r,2}YO_{n,m} \end{bmatrix} \begin{bmatrix} H_m^{\text{sc}} \\ Q_m^{\text{sc}} \end{bmatrix} = \begin{bmatrix} -ZI_{n,m} & \epsilon_{r,1}YI_{n,m} \\ 0 & 0 \end{bmatrix} \times \begin{bmatrix} H_m^{\text{inc}} \\ Q_m^{\text{inc}} \end{bmatrix}, \tag{B7}$$

where $\epsilon_{r,1}$ and $\epsilon_{r,2}$ are the relative permittivities of regions I and O, respectively, and $Q_m^{\text{sc}} = \partial H_m^{\text{sc}}(\mathbf{r}')/\partial\hat{n}$ and $Q_m^{\text{inc}} = \partial H_m^{\text{inc}}(\mathbf{r}')/\partial\hat{n}$. The analysis for perfect conductors is presented in the next subsection.

B. Boundary Element Method for Conducting Diffractive Optical Elements

The analysis presented above is applicable to both dielectrics and imperfect conductors. As presented in Section 2 in the body, for perfect conductors the integral equations reduce to a single equation in the exterior region,

$$\mathbf{E}^{\text{inc}}(\mathbf{r}_s) = \frac{\omega\mu}{4}\int_C \mathbf{J}(\mathbf{r}')H_0^{(2)} \times \left(\beta_O\sqrt{(x_s - x')^2 + (y_s - y')^2}\right)\mathrm{d}l', \quad \mathbf{r}_s \in C, \tag{B8}$$

where the two-dimensional Green's function, Eqs. (A4), has been used and the position vectors $\mathbf{r}_s(x_s, y_s)$ and $\mathbf{r}'(x', y')$ are vectors from the origin to the observation and the source point, respectively.

To determine the current distribution on the contour of the DOE, we expand the unknown surface current distribution terms of interpolation functions,

$$\hat{J}_n(\xi) = \sum_{n=1}^{N} J_n\phi_1(\xi) + J_{n+1}\phi_2(\xi), \tag{B9}$$

where again $\phi_1(\xi)$ and $\phi_2(\xi)$ are continuous functions of $\xi = [-1, 1]$ defined over a single line segment as in Eqs. (B2).

The substitution of Eqs. (B3) and (B9) into Eq. (B8) yields

$$\mathbf{E}^{\text{inc}}(x_s, y_s) = \frac{\omega\mu}{8}\sum_{n=1}^{N}\Delta l_n\int_{-1}^{1}\hat{J}_n H_0^{(2)} \times \left(\beta\sqrt{[x_s - \hat{x}_n(\xi)]^2 + [y_s - \hat{y}_n(\xi)]^2}\right)\mathrm{d}\xi, \tag{B10}$$

where again $\mathrm{d}\xi = 2\mathrm{d}l'/\Delta l_n$ and Δl_n represents the length of the corresponding line segment for element n.

To yield a discrete system of equations, we again use point matching:

$$[E_m] = [L_{m,n}][J_n] \tag{B11}$$

where

$$E_m = \mathbf{E}^{\text{inc}}(x_m, y_m), \tag{B12}$$

$$L_{m,n} = \frac{\omega\mu}{8}\int_{-1}^{1}\left\{\Delta l_n\phi_1(\xi)H_0^{(2)} \times \left(\beta\sqrt{[x_m - \hat{x}_n(\xi)]^2 + [y_m - \hat{y}_n(\xi)]^2}\right) + \Delta l_{n-1}\phi_2(\xi)H_0^{(2)} \times \left(\beta\sqrt{[x_m - \hat{x}_{n-1}(\xi)]^2 + [y_m - \hat{y}_{n-1}(\xi)]^2}\right)\right\}\mathrm{d}\xi. \tag{B13}$$

The values J_n are determined through matrix inversion of Eq. (B11), and the diffracted field values anywhere in space are determined by

$$\mathbf{E}^{\text{tot}}(x, y) = \mathbf{E}^{\text{inc}}(x, y) - \frac{\omega\mu}{8}\sum_{n=1}^{N}\Delta l_n\int_{-1}^{1}[J_n\phi_1(\xi) + J_{n+1}\phi_2(\xi)]H_0^{(2)} \times \left(\beta\sqrt{[x - \hat{x}_n(\xi)]^2 + [y - \hat{y}_n(\xi)]^2}\right)\mathrm{d}\xi. \tag{B14}$$

Equation (B14) is the BEM solution of Eq. (3) presented in Section 2.

Dennis Prather, the corresponding author, can be reached at the e-mail address prather@arl.mil.

REFERENCES

1. J. W. Goodman, *Introduction to Fourier Optics* (Wiley, New York, 1968).
2. W.-H. Lee, "Computer-generated holograms: techniques and applications," in *Progress in Optics*, E. Wolf, ed. (North-Holland, New York, 1978), Vol. XVI.
3. O. Bryngdahl and F. Wyrowski, "Digital holography—computer-generated holograms," in *Progress in Optics*, E. Wolf, ed. (North-Holland, New York, 1990), Vol. XXVIII.
4. F. Wyrowski and O. Bryngdahl, "Digital holography as part of diffractive optics," Rep. Prog. Phys. **54**, 1481–1571 (1991).
5. S.-H. Lee, ed., *Selected Papers on Computer-Generated Holograms and Diffractive Optics*, Vol. MS33 of Milestone Series (SPIE, Bellingham, Wash. 1992).
6. J. N. Mait, "Understanding diffractive optic design in the scalar domain," J. Opt. Soc. Am. A **12**, 2145–2158 (1995).
7. M. W. Farn, "Binary gratings with increased efficiency," Appl. Opt. **31**, 4453–4458 (1992).
8. E. N. Glytsis and T. K. Gaylord, "High-spatial-frequency binary and multilevel stairstep gratings: polarization-selective mirrors and broadband antireflection surfaces," Appl. Opt. **31**, 4459–4470 (1992).
9. H. Haidner, J. T. Sheridan, J. Schwider , and N. Streibl, "Design of a blazed grating consisting of metallic subwavelength binary grooves," Opt. Commun. **98**, 5–10 (1993).
10. E. Sidick, A. Knoesen, and J. N. Mait, "Design and rigorous analysis of high-efficiency array generators," Appl. Opt. **32**, 2599–2605 (1993).
11. E. Noponen, J. Turunen, and A. Vasara, "Electromagnetic theory and design of diffractive-lens arrays," J. Opt. Soc. Am. A **10**, 434–443 (1993).
12. P. Kipfer, M. Collischon, H. Haidner, J. T. Sheridan, J. Schwider, N. Streibl, and J. Lindolf, "Infrared optical components based on a microrelief structure," Opt. Eng. **33**, 79–84 (1994).
13. M. Schmitz, R. Brauer, and O. Bryngdahl, "Phase gratings with subwavelength structures," J. Opt. Soc. Am. A **12**, 2458–2462 (1995).
14. See feature section, "Diffractive Optics Modeling," J. Opt. Soc. Am. A **12**, 1025–1169 (1995).
15. D. W. Prather, M. S. Mirotznik, and J. N. Mait, "Boundary element method for vector modeling diffractive optical elements," in *Diffractive and Holographic Optics Technology II,* I. Cindrich and S.-H. Lee, eds., Proc. SPIE **2404**, 28–39 (1995).
16. R. F. Harrington, *Field Computation by Moment Methods* (Krieger, Malabar, Fla., 1968).
17. F. Princemin, A. Sentenac, and J. J. Greffet, "Near field scattered by a dielectric rod below a metallic surface," J. Opt. Soc. Am. A **11**, 1117–1127 (1994).
18. R. Petit, ed., *Electromagnetic Theory of Gratings* (Springer-Verlag, Berlin, 1980).
19. D. Maystre, "Rigorous vector theories of diffraction gratings," in *Progress in Optics*, E. Wolf, ed. (North-Holland, New York, 1984), Vol. XXI.

20. B. Kleeman, A. Mitreiter, and F. Wyrowski, "Integral equation method in diffractive optics," presented at the Workshop on Diffractive Optics, Prague, Czech Republic, August 1995.
21. H. El-Mikati, and J. B. Davies, "Improved boundary element techniques for two-dimensional scattering problems with circular boundaries," IEEE Trans. Antennas Propag. **AP-35**, 539–544 (1987).
22. N. Morita, N. Kumagai, and J. R. Mautz, *Integral Equation Methods for Electromagnetics* (Artech, Norwood, Mass., 1991).
23. A. Ishimaru, *Electromagnetic Wave Propagation, Radiation, and Scattering* (Prentice-Hall, Englewood Cliffs, N.J., 1991), pp. 195–199.
24. S. Kagami and I. Fukai, "Application of boundary-element method to electromagnetic field problems," IEEE Trans. Antennas Propag. **AP-32**, 455–461 (1984).
25. K. Yashiro and S. Ohkawa, "Boundary element method for electromagnetic scattering from cylinders," IEEE Trans. Antennas Propag. **AP-33**, 383–389 (1985).
26. P. D. Maker, D. W. Wilson, and R. E. Muller, "Fabrication and performance of optical interconnect analog phase holograms made by electron beam lithography," in *Optoelectronic Interconnects and Packaging*, Vol. CR62 of Critical Reviews Series, R. T. Chen and P. S. Guilfoyle, eds. (SPIE, Bellingham, Wash., 1996), pp. 415–430.
27. B. Lichtenberg and N. C. Gallagher, "Numerical modelling of diffractive devices using the finite element method," Opt. Eng. **33**, 3518–3526 (1994).
28. M. S. Mirotznik, D. W. Prather, and J. N. Mait, "A hybrid finite element–boundary element method for the analysis of diffractive elements," J. Mod. Opt. **43,** 1308–1321 (1996).
29. J. L. Yao-Bi, L. Nicolas, and A. Nicolas, "2D electromagnetic scattering by simple shapes: a quantification of the error due to open boundary," IEEE Trans. Magn. **29**, 1830–1834 (1993).
30. B. Stupfel and R. Mittra, "A theoretical study of numerical absorbing boundary conditions," IEEE Trans. Antennas Propag. **43**, 478–486 (1995).
31. J. J. Wang, *Generalized Moment Methods in Electromagnetics* (Wiley, New York, 1991).
32. T. K. Gaylord and M. G. Moharam, "Analysis and applications of optical diffraction by gratings," Proc. IEEE **73**, 894–937 (1985).
33. C. B. Burchkardt, "Diffraction of a plane wave at a sinusoidally stratified dielectric grating," J. Opt. Soc. Am. **56**, 1502–1509 (1966).
34. F. G. Kasper, "Diffraction by thick, periodically stratified gratings with complex dielectric constant," J. Opt. Soc. Am. **63**, 37–45 (1973).
35. K. Knop, "Rigorous diffraction theory for transmission phase gratings with deep rectangular grooves," J. Opt. Soc. Am. **68**, 1206–1210 (1978).
36. C. A. Balanis, *Advanced Engineering Electromagnetics* (Wiley, New York, 1989).
37. J. J. Stammes, "Focusing of two-dimensional waves," J. Opt. Soc. Am. **71**, 15–31 (1981).
38. J. Jin, *The Finite Element Method in Electromagnetics* (Wiley, New York, 1993).
39. M. Abramowitz and I. A. Stegun, eds., *Handbook of Mathematical Functions* (Dover, New York, 1970), p. 360.